Coastal Engineering 118 (2016) 35–49

Contents lists available at ScienceDirect

Coastal Engineering

journal homepage: www.elsevier.com/locate/coastaleng

Experimental analysis of debris motion due the obstruction from fixed obstacles in tsunami-like flow conditions

N. Goseberg [a,b,*], J. Stolle [b], I. Nistor [b], T. Shibayama [c]

[a] Leibniz University Hannover, Welfengarten 1, Hannover, Germany
[b] Department of Civil Engineering, University of Ottawa, 75 Laurier Avenue East, Ottawa, Canada
[c] Department of Civil and Environmental Engineering, Waseda University, 1 Chome-104 Totsukamachi, Shinjuku, Tokyo, Japan

ARTICLE INFO

Article history:
Received 25 April 2016
Received in revised form 16 August 2016
Accepted 24 August 2016
Available online 16 September 2016

Keywords:
Debris
Debris motion
Obstacles
Tsunami
Coastal engineering
Debris tracking

ABSTRACT

Experimental research was conducted focusing on debris motion over a horizontal apron featuring vertical obstacles in the path of the debris propagation. The apron was designed as a typical representation of a harbor threatened by an inundating tsunami. The experimental setup idealized often complex harbor settings. The debris was a scaled-down 20-foot shipping container modelled at a 1 in 40 Froude length scale. Offand onshore regions were separated by a vertical quay wall which allowed the incoming elongated solitary wave used to represent the first part of a tsunami to steepen, break and propagate over the initially dry surface as a tsunami-like bore. In the path of propagation, a varying number of debris were entrained within the inundating bore over the horizontal apron. The entrained debris interacted with regularly spaced vertical obstacles representing infrastructure and houses within the propagation path. Varying debris and obstacle arrangements were tested to evaluate the effects the obstacles would have on the debris' maximum longitudinal displacement and the spreading angle. The main conclusion is that the spreading angle of the debris is not as significantly altered by the presence of obstacles on the harbor apron whereas the maximum longitudinal displacement of the debris was significantly affected.

1. Introduction

Over the past several decades, major tsunami events, such as the 2004 Indian Ocean tsunami, the 2010 Chilean tsunami, and the 2011 Tohoku tsunami have been responsible for catastrophic damage to local communities and associated infrastructure near the shoreline as well as unprecedented loss of human lives. The damage was often due to the lack of necessary capacity for structures to sustain the extreme forces associated with the inundating tsunami bore (Ghobarah et al., 2006; Palermo et al., 2009, 2013; Yeh et al., 2014; Esteban et al., 2015). Among numerous reasons, the loss of life is often attributed to low levels of preparedness, missing or inadequate evacuation routes or available shelter infrastructure. To date, there is still major uncertainties related to the proper design of evacuation shelters against hydrodynamic loading, random debris impact forces, debris damming, and scouring processes occurring at various instants over the run-up and run-down sequence. However, the American Society of Civil Engineering (ASCE) Standards Subcommittee on *Tsunami Loads and Effects* (of which the third author is a member) is currently developing a new chapter in the 2016 release of the ASCE7 standard which aims to remedy some uncertainty involved in the design process related to buildings located in tsunami-prone regions through condensed stipulations in mandatory language.

According to the Federal Emergency Management Agency (FEMA) P-646 design guideline (2012), many large scale tsunamis break in shallow waters, forming a *tsunami bore* which is characterized by a violently foaming, turbulent and steep wave front propagating on top of the much longer main tsunami wave in finite water depth. The breaking is predominant for leading elevation waves and occurs as a result of wave shoaling and non-linear transformations over the continental shelfs (Yeh, 2009). At the shoreline, the tsunami bore continues propagating on-shore due to its momentum and is thereafter termed a *tsunami bore*. A second or third tsunami wave crest, which in some cases could be larger than the first one, could spread inland as a tsunami bore (now over a wet bed) as the first wave has already inundated initially dry land. Therefore it is paramount to define the design loads based on these two hydrodynamic conditions, namely tsunami bores travelling over a wet bed and tsunami bores propagating over dry ground.

Many structures are not properly designed against such extreme hydrodynamics as many guidelines do not address the issue of tsunami loading explicitly (Palermo et al., 2009; Esteban et al., 2014; Yeh et al., 2014). Guidelines and standards, such as FEMA P55 (FEMA P-55, 2011) and ASCE7 Chapter 5 (Coulbourne, 2011), focus primarily on

* Corresponding author.
E-mail addresses: contact@nilsgoseberg.de (N. Goseberg), jstol065@uottawa.ca (J. Stolle), inistor@uottawa.ca (I. Nistor), shibayama@waseda.jp (T. Shibayama).

http://dx.doi.org/10.1016/j.coastaleng.2016.08.012
0378-3839/

coastal flooding and only briefly mention the extreme loading conditions resulting from tsunami. The *National Building Code of Canada* (*NBCC*) (*2005*) acknowledges in its "Design for seismic effects" that the damage from earthquakes can be a result of a tsunami but lacks to provide guidelines regarding the potential loading conditions (Palermo et al., 2009). Due to the tragic loss of life and major economic losses, research groups and governing bodies world-wide have begun to focus on better understanding the loading conditions on structures due to tsunami bores and bores.

The primary focus of the existing research has been on the hydrodynamic loading as a result of the inundating tsunami bore and a number of load estimations for hydrodynamic loading were proposed (Ramsden, 1996; Arnason et al., 2009; Nouri et al., 2010; St-Germain et al., 2012; Chinnarasri et al., 2013; Wei et al., 2015). However, in forensic engineering site surveys of affect coastal communities, significant secondary damage has been observed from debris entrained within the bore (Ghobarah et al., 2006; Palermo et al., 2009, 2013; Takahashi et al., 2010; Naito et al., 2014). Despite the prevalence of debris impact, significantly less work has gone into the study of these loading conditions and the most significant gap in the understanding of debris impact is the nature of the debris motion within the inundating bore. The study of debris motion has been difficult as a large number of variables, such as flow conditions (Matsutomi, 2009), debris physical characteristics (Imamura et al., 2008; Matsutomi, 2009; Shafiei et al., 2014), surrounding environment (Naito et al., 2014; Rueben et al., 2014) and many more, have significant roles in affecting the debris motion.

To date, scarce research exists that addresses the initiation of debris motion and the entrainment process of multiple debris within reach of a rapid flow. Clearly, sound understanding of the entrainment process, the subsequent transport path and downstream debris concentration are paramount to assess the downstream debris impact hazard. Changes to a dam break wave bore front under dry and wet bet conditions were studied by Khan et al. (2000), who identified the governing parameter for the debris influence on the bore height and celerity to be the ratio of concentration of the mass of the particles to the mass of water upstream of the gate (concentration ratio), and the ratio of the size of the particles relative to the upstream depth (length ratio). High concentration of debris downstream of the gate position resulted in increased bore heights. This observation suggests that besides additional impact loads stemming from the debris entrained in the flow, higher hydrodynamic loads could be expected on structures present in the leeward reach of such flows. Haehnel and Daly (2004) investigated impact forces of single woody debris in flume and basin tests and developed a single-degree-of-freedom model to estimate their impact force, given an upper envelop value of effective contact stiffness between the debris and a rigid structure. It is however unclear how impact forces would develop in the likely case of multiple impact of debris, even under the assumption that not all impacts would occur under a flow-wise directed angle of impact. In this regard, it is again of paramount interest to understand how debris are entrained within a transient flow and how they disperses along its path of transport. On the temporal scale, it is still undetermined how likely it is that hydrodynamic and impact forces occur synchronously and, thus, how load combinations for a practical design should be considered. From experiments involving dam break waves (Arnason et al., 2009; Nouri et al., 2010), it could be conjectured that a time lag exists between the arrival of the bore front and the debris impact. So far, it was however not investigated how this time lag changes over the propagation time elapsed since debris entrainment and for various distances between the original debris site and the impact position. A recent in-situ study on river ice runs suggests that the water wave front of the dam break following a sudden breach of an ice-jam outruns the ice phase by some jam length (Nafziger et al., 2016). A study involving single pieces of wooden logs constrained within a flow-normal motion directly in front of a vertical structure concluded that impact forces may show single peaks which significantly increased overall base shear forces (Nistor et al., 2011); in some experiments however, double peaks resulted from a bounce back effect, the infrequent occurrence of these events point to some degree of randomness involved in the experimental design. This finding stresses the need for better knowledge about the debris motion and entrainment at first in order to assess impact loads accurately.

In addition to floating debris, debris entrained within incoming tsunami waves or bores could also consist of negatively buoyant material originating from dislodged and subsequently dismantled residential or community houses. These high-density, heavier debris could result in design-relevant impact events attacking neighboring infrastructure at lower-lying load carrying points compared with their floating counterpart debris entrained at the free surface of the flow. Transport modes of negatively-buoyant debris in the form of boulders were found to be sliding, rolling and saltation in bore-type flows (Imamura et al., 2008); a more recent study by Zainali and Weiss (2015) however revealed that factors such as the submergence ratio, the boulder geometry and weight as well as their aspect ratios form a complex, non-linear parameter space which defines the dislodgement distance, clearly pointing out the difficulties involved in predicting such processes.

Naito et al. (2014), in a forensic site survey following the 2011 Tohoku Tsunami, developed a simple procedure for determining the spreading angle of debris using satellite images. From this analysis, Naito et al. (2014) noticed that the environment surrounding the debris significantly affected its overall displacement and therefore its potential to impact critical structures and infrastructure. In an experimental attempt to verify estimates of debris spreading, Nistor et al. (2016) experimentally investigated debris spreading over a horizontal apron, neglecting the specific influences of rigid obstacles in the path of the debris. While the spreading angles and total inland displacement were empirically quantified by linear relationships, the effects of the interaction of debris with obstacles located in their path were left for further investigation and make the object of this paper. Debris in built areas would be obstructed by surrounding buildings, assuming the buildings are not destroyed by the tsunami bore or resulting debris impact. These obstructions severely limit the displacement of the debris rendering further research regarding the influence of rigid structures (named obstacles hereafter) on the dispersal of debris in extreme hydrodynamic flows necessary. The effect of obstacles in the pathway of debris on its dispersal has not been investigated before. These effects however deserves particular attention as planners and designers of risk-prone harbor infrastructure require reliable information on how debris spread through the nearshore area and which of the potential buildings lie within debris-impact zones.

Based on the above rationale, the objectives of this paper are to specifically examine:

1) The reciprocal effect of rigid obstacles residing on a horizontal harbor area on the hydraulic conditions of an incoming tsunami bore.
2) The associated effect of the rigid obstacles on the motion of debris of varying count by modelling debris consisting 20-foot shipping containers.
3) The characteristics of the overall motion of the debris influenced by rigid obstacles compared to conditions where no obstacles are present on the harbor area.
4) Whether the presence of obstacles affects and alters trajectories of propagating debris, their overall spreading angles and maximum longitudinal displacements.
5) The method to determine inertial forces exerted on the debris during the initial contact with the incoming wave front and the subsequent impact forces exerted on the obstacles by the moving debris.

This paper is outlined as follows: the "Experimental Setup" introduces the Waseda Tsunami Wave Basin, instrumentation, and the tracking system used in the experiments; the "Results" section presents the analysis performed on the hydrodynamics, debris motion and debris impact; the "Discussion" analyzes the results and places the current work in the context of previous research efforts; "Conclusions" outline

the key findings of this study and examines the potential next steps in examining the effect of obstacles on debris motion.

2. Experimental setup

2.1. Tsunami Wave Basin

The experimental research reported herein was part of a larger series of tests conducted in the Coastal Engineering and Management Laboratory at the Department of Civil Engineering of Waseda University in Tokyo, Japan. A recently constructed rectangular Tsunami Wave Basin (TWB) was used. The TWB had horizontal dimensions of 4-by-9 m, as shown in Fig. 1. On the North side of the TWB, a wave maker was installed whose operation is based on releasing a volume of water with a defined head with respect to the still water depth of the basin. After initializing the release of the water, the reservoirs emptied under the influence of gravity. A flow characterized by a solitary wave front profile, though extended with an elongated tail flow, was generated. A more detailed description of the wave maker and the wave basin features is provided in Nistor et al. (2016). A horizontal rigid apron area modelling a port environment with container handling facilities was constructed opposite to the wave maker and covering slightly more than half of the length of the TWB. The flat, horizontal bottom was chosen to conservatively investigate the longitudinal displacement of the debris. A positive slope would result in a reduced longitudinal displacement of the debris as the onshore inundation limit of the tsunami wave would be reduced (Dias and Dutykh, 2007). Additionally, factors such as surface roughness and topography, would influence the debris propagation (Bocchiola et al., 2006). However, the influence of these factors is difficult to consider at model scale and tends to be site-specific. The present experimental setting was kept simple in an attempt to minimize the influence of such factors.

The generated waves propagated across the TWB, as indicated in Fig. 1, in blue colour. A vertical wall representing a quay wall separated the wave propagation section and the horizontal harbor apron area; a freeboard of 1.5 cm existed between those two sections. The origin of

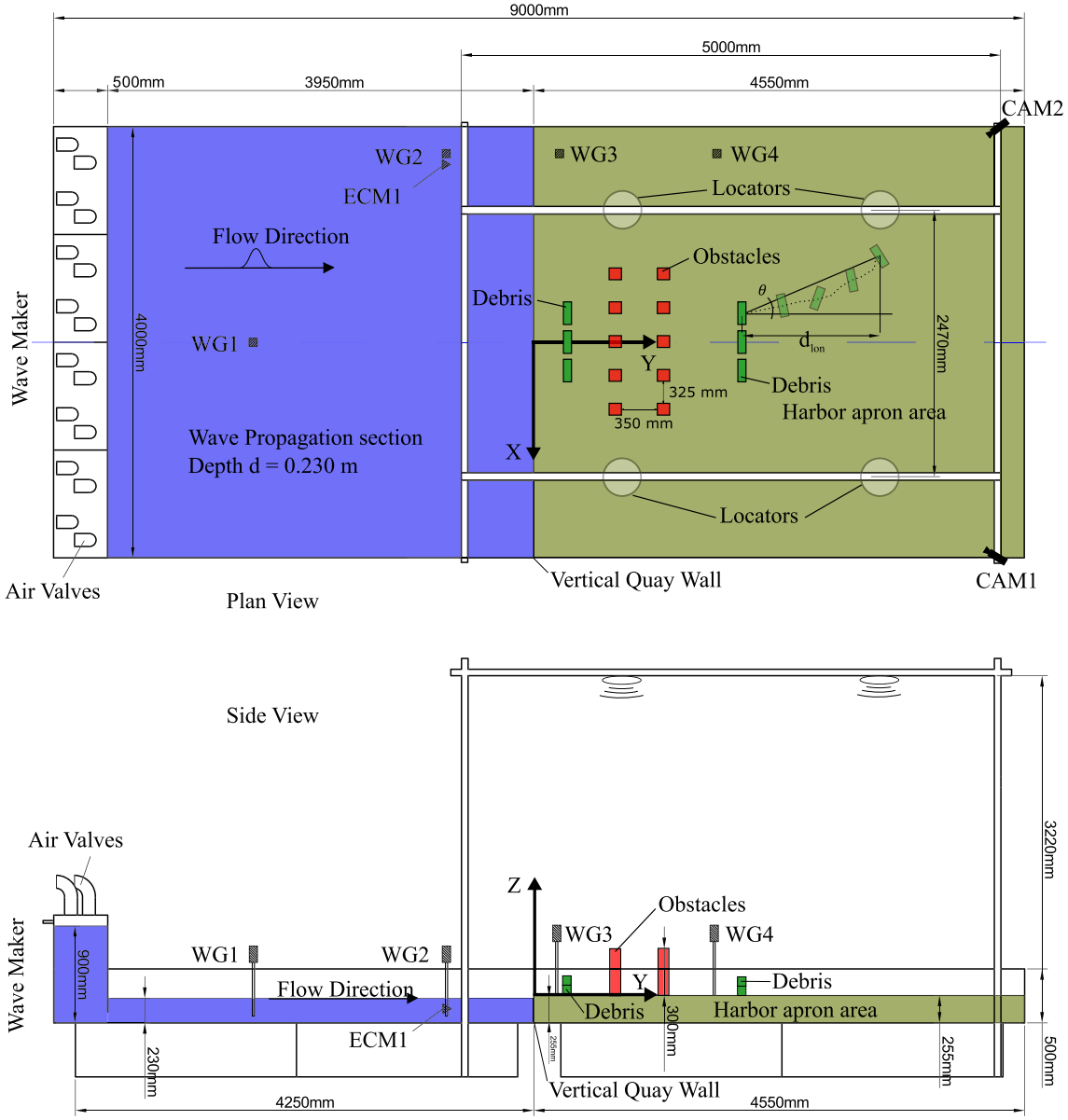

Fig. 1. Tsunami Wave Basin (TWB). The blue area is the wave propagation section, the brown section is the harbor apron area. The red squares are the fixed obstacles, the light grey ones are the wave gauges, and the white circles are the locators used in the Real-time Locating System. Green squares indicate positions of debris.

the right-handed coordinate system used throughout the tests resided at the midpoint of the uppermost apron edge with the positive y-axis pointing inland. The z-axis pointed positively upwards opposite to the vector of gravity.

2.2. Instrumentation

Fig. 1 also depicts the instrument positions within the TWB which were used to record water levels, velocities, taking photographs and aiding the collection of positional information of the individual container models. A summary of instrument positions, IDs and sampling rates is provided in Table 1.

Two capacitance-type wave gauges (WG, manufactured by Kenek, Japan) were placed in the wave propagation section while the remaining two capacitance-type wave gauges were placed along the initially dry harbor apron area. Close to the position of the wave gauge WG2, an electro-magnetic current meter (ECM, also by Kenek, Japan) was installed with its sensor head submerged 0.07 m below the still water level ($z = -0.085$ m). Thorough calibration of the equipment yielded correlation coefficients above 0.99 for the entire calibration process. The apron area was additionally monitored using two high-definition (HD) cameras (pi1900-32gc, manufacturer: Basler AG, Germany) pointed towards the apron's edge, the debris site and the obstacles; the coverage allowed to analyze the propagation of the tsunami bore front over the apron edge, the debris site and the flow through the obstacles at a sampling frequency of 25 Hz. Four locator antennae were installed below a rigid frame which belonged to a real-time location system capable to track up to 25 individual debris across the physical domain. The real-time location system (RTLS) is part of a six-degree-of-freedom (6DOF) "Smart" debris system which is further detailed in the next section.

2.3. "Smart" debris system

"Smart" debris, described in more detail in Goseberg et al. (2016), were used to track the container models across the physical domain. 20-foot shipping containers (modelled based on the ISO 668/688 standard) were chosen as the debris. The containers were down-scaled (Froude similitude, dimensions $0.06 \times 0.06 \times 0.15$ m, length scale 1:40) and batch-produced for assuring identical dimensions and weights of a positively buoyant polyethylene (PE-HMW, 0.92 g/cm^3), as shown in Fig. 2. The total weight of a single container model was determined by three repeated weighing which yielded an average total weight of 0.226 kg which included one motion sensor (0.048 kg) and one location tag (0.010 kg). Herein, a target prototype container weight of $W = 14{,}400$ kg (Knörr and Kutzner, 2008) was chosen to model average fully-loaded shipping containers. An approximate uniform draft of 0.025 m was thus achieved. Smaller or larger container weights could potentially influence the maximum longitudinal distance which a container may travel or its spreading angle after being entrained in a tsunami wave or bore. However, to date, it is unclear what statistical weight distribution most of the worldwide-used containers follow. Thus, the approach chosen herein assumes that not all of the containers trade on the maximum load capacity in order to prevent too conservative results in terms of maximum longitudinal distance and spreading angle of the debris. To maintain uniformity between the test cases, the debris were placed with the heavier side (the side with the accelerometers) on the apron for each test.

The positional information in the two horizontal dimensions of the 6DOF "Smart" Debris system (Goseberg et al., 2016) was used to track the container models as they moved across the harbor apron area. The three rotational motions were also recorded by means of a motion sensor (3-Space Logging, manufacturer: Yost Eng. USA) though not analysed herein, but instead the acceleration data also recorded were used to determine inertial forces. The positional information were collected as part of the "Smart" debris system by the RTLS (manufacturer: Quuppa Oy, Finland) employing trilateration by means of a Bluetooth Low Energy (BLE) wireless connection between the locators shown in Fig. 1 and a single locator tag as shown in Fig. 2(a) (inside front half of the container). Container models were labeled individually at one corner for identifying each particular "Smart" Debris and the containers' orientation during their initial placement on the harbor apron. The total weight of a single container model was determined by three repeated weightings which yielded an average total weight of 0.226 kg which included one motion sensor (0.048 kg) and one location tag (0.010 kg).

2.4. Container models initial arrangements and fixed obstacle positions

Reconnaissance missions in the aftermath of severe tsunamis oftentimes found that displaced shipping containers (Okal et al., 2010; Naito et al., 2014) constitute an imminent threat to infrastructure positioned farther inland of the debris' initial position. The scaled-down 20′ shipping containers were designed to provide shelter and water-protection to the "Smart" debris system. Variability of harbor infrastructure such as buildings or warehouses is inherently difficult to mimic in hydraulic scale models due to its various configurations, count and spacing. As a first-order approximation of those variations, obstruction by such infrastructure occurring in the pathway of entrained debris is modelled by one and two rows of equidistantly-spaced square cuboids which were positioned in fixed positions, parallel to the harbor apron edge. Table 2 lists the experimental runs conducted in this study outlining the debris and obstacle arrangement principles and key positions.

For the cases where "Downstream" was indicated in Table 2, the debris were placed downstream of the fixed obstacles, at a distance of $y = 1.81$ m.

Fig. 3(a) shows a photograph of the debris and obstacle arrangement C4, depicting the two rows of obstacles made of fixed wooden square blocks with a width in x- and y-direction of 0.10 m and a height of 0.2 m. The spacing between the two centerlines of the rows in the y-direction was of 0.45 m. The centerline spacing in the lateral direction (x) was of 0.325 m, leading to an opening width in between the

Table 1
Instrumentation used in the experimental tests.

Instrument name	Instrument ID tag	X [m]	Y [m]	Z [m]	Sampling rate [Hz]	Notes
WG1	CHT6-30-1	0.00	−2.60	–	100	
WG2	CHT6-30-2	−1.75	−0.81	–	100	
WG3	CHT6-30-3	−1.75	0.24	–	100	
WG4	CHT6-30-4	−1.75	1.70	–	100	
ECM1(X)	VMT2-200-04P	−1.65	−0.81	−0.10	100	Collocated with WG2
ECM2(Y)	VMT2-200-04P	−1.65	−0.81	−0.10	100	Collocated with WG2
CAM1	pi1900-32gc	2.00	4.20	2.95	25	Pointed to area of interest
CAM2	pi1900-32gc	−2.00	4.20	2.95	25	Pointed to area of interest
LOC1	9			3.15	22–48	Downward looking
LOC2	10			3.15	22–48	Downward looking
LOC3	11			3.15	22–48	Downward looking
LOC4	12			3.15	22–48	Downward looking

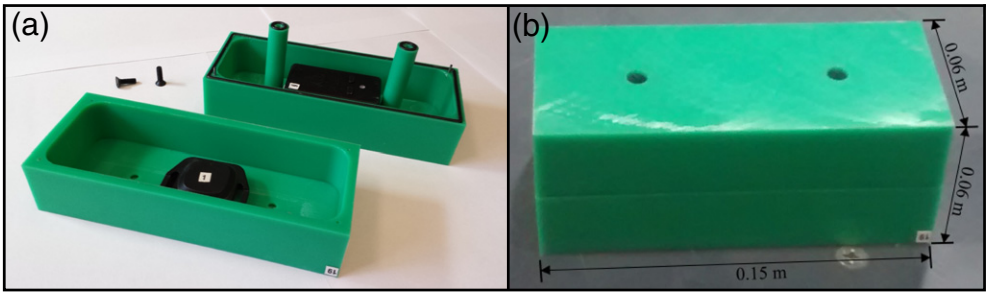

Fig. 2. "Smart" debris: scaled-down (1:40 Froude scaling) shipping container made of polyethylene (PE). (a) open "Smart" Debris with BLE tag and motion sensor. (b) closed "Smart" debris model.

obstacles of 1.5 times the longest container dimension (0.225 m). This ratio was estimated based on previous research which suggests that the likelihood of jamming is positively correlated with the ratio of debris length to opening width (Bocchiola et al., 2006; Rusyda et al., 2014); the chosen ratio avoided thus debris jamming during the experiments. For the cases where "Downstream" was indicated in Table 2, the debris were placed downstream of the fixed obstacles, at a distance of y = 1.81 m.

For the cases where "Downstream" was indicated in Table 2, the debris were placed downstream of the fixed obstacles, at a distance of y = 1.81 m.

Fig. 3(b)–(f) depict the container models initial arrangements and obstacles' positions. Container model arrangements with 3-by-1 container rows with the longer container side parallel to the apron edge were investigated in one- and two-layer stack arrangements. In addition, the same container model arrangement was used by positioning them downstream of the obstacles to test how the reduced flow velocity affected the debris spreading. For more details about the modelling and arrangements of the containers, the reader is referred to Stolle et al. (2016) and Nistor et al. (2016). Center of volume positions of the containers are listed in Table 2. Inter-container spacing was chosen to be 0.03 m which translates to 1.20 m in prototype based on the assumption that this is a minimum space requirement for common gantry cranes and stacking equipment. Spacing between container models was kept constant throughout the experiments. Although standardized container storage operations allows stacking heights of 5 or more layers, the total number of container model and obstacle arrangements had to be restricted for practical considerations. Herein, up to 6 container models and up to 2 layers were chosen. The distance between the first row of containers and the harbor apron was set to 0.20 m (8.00 m in prototype, apron edge to front face edge of debris) based on the assumption that trains and trucks need space for operation between the stacking grounds and the existing quay walls in praxis.

2.5. Experimental procedure

Still water depth in the TWB was always set to 0.230 m in the wave propagation section, as indicated in Fig. 1. During the tests reported herein, the hydraulic head inside the wave maker's reservoir chambers was initially set at 0.665 m. The reservoir chambers were filled by means of a vacuum pump and it was controlled such that identical hydraulic conditions were met before engaging the wave maker and releasing the water volume. All sensors and instruments were activated prior to a start of an experimental run. Particular attention was given to the "Smart" debris sensors which had to be inserted inside the container model, sealed, and then placed according to the container model arrangement outlined in Table 2. Adhesive forces between the containers were kept relatively constant by drying each of the containers after an experimental run such as they would not affect debris dynamics during the motion initiation. Placement of the container models was facilitated by position markers on the harbor apron surface and spacers were used to ensure accurate gap spacing in between the container models. Placement accuracy of ± 5 mm was achieved following this procedure. Finally, the wave maker was started by synchronously opening the air valves which held the water volume inside the reservoir chambers prior to experiment start. Synchronization between the computers and systems used was guaranteed through the use of a Network Time Protocol (NTP) server which was installed on the computer controlling the RTLS system. Synchronization accuracy of 30 ms was reported by the NTP server.

3. Results

3.1. Hydrodynamics of the elongated solitary wave

Surface elevation and the horizontal particle velocity at a point 0.07 m below the still water surface time-histories are shown in Fig. 4 for a baseline test run (#1, in red), as well as for the subsequent tests with one (#28, in blue) and two (#32, in green) rows of obstacles; measured time-histories are compared with theoretical results of a solitary wave following Munk (1949). The theoretical surface elevation time-history $\eta(y,t)$ at a certain position y along its axis of propagation is expressed as follows:

$$\eta(y,t) = H \cdot sech^2(k \cdot (tC - y)) \quad (1)$$

Table 2
The categories used in specifying the type of experiments used to evaluate the motion of the debris with the presence of fixed obstacles. Positions refer to center of volume of container models and obstacles.

ID	Category	Number of debris	Position of debris in Y-direction [m]	Position of obstacles in Y-direction [m]	Experimental runs [#]
C01	No obstacles	3	0.23	–	9, 11, 12, 13, 14, 15
C02		6	0.23	–	43, 44
C03	No obstacles (downstream)	6	1.81	–	45, 46
C1	One row of obstacles	3	0.23	0.71	28, 29
C2		6	0.23	0.71	30, 31
C3	Two rows of obstacles	3	0.23	0.71	32, 33
C4		6	0.23	0.71, 1.16	34, 35, 36, 37, 38, 39
C5	Two rows of obstacles (downstream)	6	1.81	0.71, 1.16	40, 41, 42

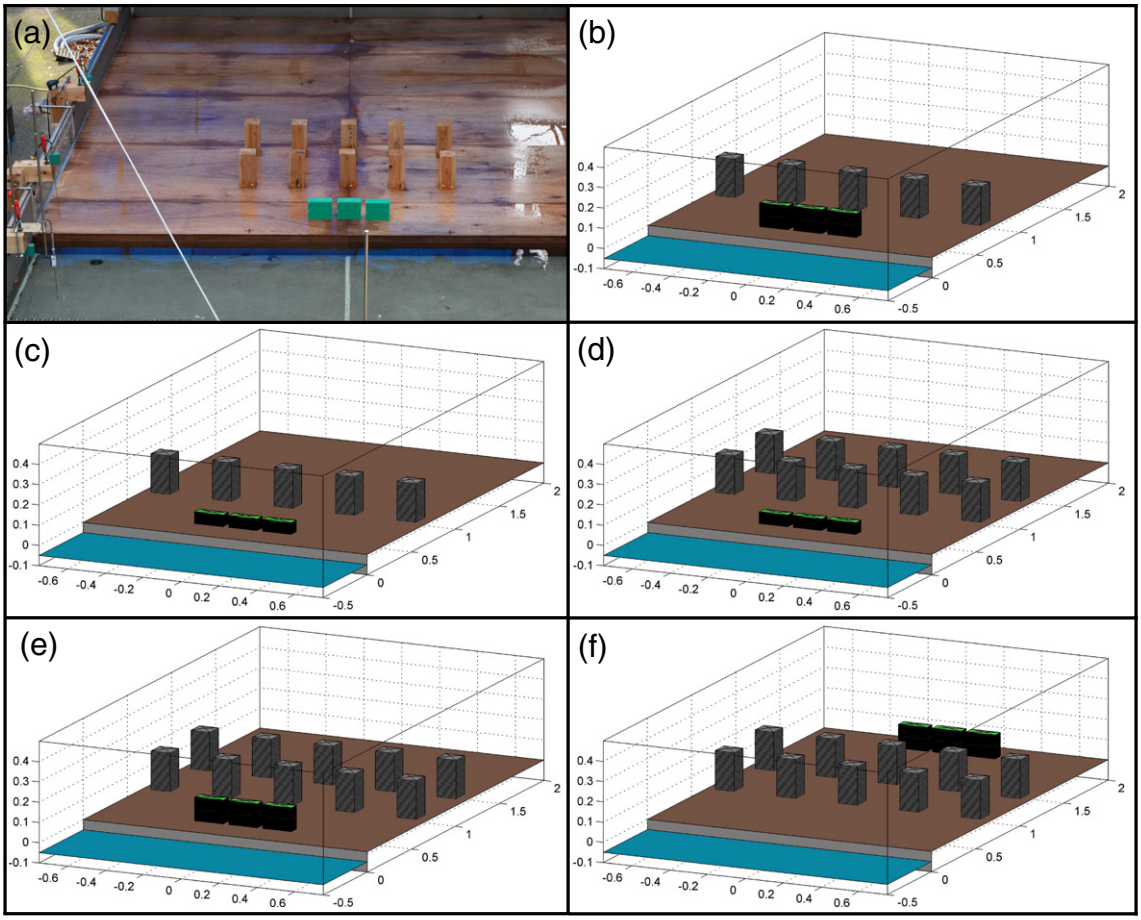

Fig. 3. (a) Photograph of one experimental setup. (b)–(f) Container Model Initial Arrangements and Obstacle Positions used for the experiments, wave arrival from the front of the figure panels.

with H being the wave amplitude, wave number $k = \sqrt{3H/4h}$, h being the water depth, and wave celerity $C = \sqrt{g \cdot (h + H)}$. Tests shown here all had an instantaneous opening time of the air valves of the wave maker and instrument positions are indicated in Fig. 1. All times are referenced to the instant when the wave motion was initiated. Time-history of the water surface elevation at a distance of 1.35 m away from the wave maker is shown in The presence of the vertical quay wall and the nonlinear dynamics of the elongated solitary wave train induced a wave height increase at the leading wave front (approximately 34%), along with an increase in its steepness and subsequent breaking.

Fig. 4(a). As shown, the surface profile of the wave front is in good agreement with the theoretical solitary wave solution. However, in

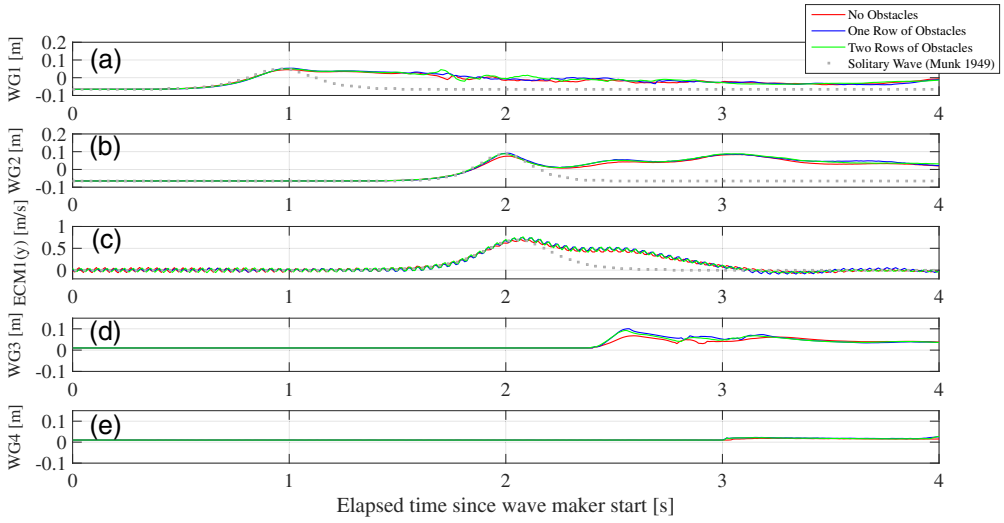

Fig. 4. Time-history of the wave front profiles at the wave gauges (WG) and the time-history of the horizontal orbital velocity measured with the electro-current meter (ECM). No obstacles (red), one row of obstacles (blue), and two rows of obstacles (green) are compared to the analytical solution of (Munk, 1949).

contrast to the later, the observed surface elevation at WG1 exhibits an elongated tail which is sustained by the excess volume of water flowing out of the reservoir chambers exceeding the required volume to generate an ideal solitary wave tail. The presence of the vertical quay wall and the non-linear dynamics of the elongated solitary wave train induced a wave height increase at the leading wave front (approximately 34%), along with an increase in its steepness and subsequent breaking.

The duration of the entire wave was approximately 4.5 s compared to a duration of the solitary wave of ~1.3 s based on the duration definition by Madsen et al. (2009). The wave duration achieved in the current tests translates to wave periods at prototype conditions of 28.5 s. Results from the wave gauge WG2, which was located close to the apron, are shown in The presence of the vertical quay wall and the non-linear dynamics of the elongated solitary wave train induced a wave height increase at the leading wave front (approximately 34%), along with an increase in its steepness and subsequent breaking.

Fig. 4(b) which includes the partial reflection occurring at the vertical quay wall (the second smaller peak) separating the wave propagation section from the harbor apron area. The good agreement between the theoretical and the observed water levels is well maintained at this wave gauge as well. Results from the wave gauges WG3 and WG4 are shown in The presence of the vertical quay wall and the non-linear dynamics of the elongated solitary wave train induced a wave height increase at the leading wave front (approximately 34%), along with an increase in its steepness and subsequent breaking.

Fig. 4(d) and (e), respectively. The presence of the quay wall and the non-linear dynamics of the incoming elongated solitary wave results in strong amplification which induces a breaking over the apron edge. Horizontal particle velocity time-series $u_H(z,y,t)$ under a solitary wave at a non-dimensional depth $Z = z/h$ and travelled distance $Y = y/h$ is theoretically defined by Munk (1949) as

$$u_H(y,z,t) = CN\left(\frac{1+\cos(MZ)\cosh(MX)}{(\cos(MZ)+\cosh(MX))^2}\right) \quad (2)$$

with M and N being tabulated function values depending on the wave amplitude, H. The presence of the vertical quay wall and the non-linear dynamics of the elongated solitary wave train induced a wave height increase at the leading wave front (approximately 34%), along with an increase in its steepness and subsequent breaking.

Fig. 4(c) compares the theoretical horizontal orbital velocity under a solitary wave with the observed velocity time-history and excellent agreement is found for the front branch of the solitary wave. Maximum (peak) velocity measured in the experiments is 0.8 m/s. Due to the solitary wave elongation, the velocity time-history lasts at least twice as long as the theoretical counterpart which in the sequel of its propagation allows for extended transport of debris across the harbor apron area as the tsunami-like bore breaks and bores inland.

At the same time, it becomes apparent that the presence of obstacle rows of the chosen spatial distribution on the apron has negligible effects on the time-histories of the water surface elevation at the WG positions. As the WG were placed along the wall of the apron, the effect of the obstacles could not be observed due to the relative large width of the TWB. While at WG1, some differences between the experimental and theoretical solution water surface occur between time 2.0 and 3.0 s, peak water levels are slightly increased at WG3 at time 2.6 s for the cases with obstacles present. Apart from these minor differences, there is good agreement between the experimental runs with and without the obstacle's presence on the apron. Hence, this ensures that the hydrodynamic conditions are comparable across the experimental runs.

3.2. Bore front profile analysis

While the effect of the obstacles cannot be quantitatively observed in the results of the WG data, a second approach was carried out to evaluate the effect of the obstacles on the hydrodynamic conditions. The bore front profile for the following analysis is defined as the location of the wetting front moving over the dry ground on the harbor apron area. The bore front profile analysis was manually performed to evaluate the change in the bore front velocity as the bore propagates through the obstacle rows. The bore front profile analysis was performed by manually selecting the bore front in each image. An accuracy of ± 10 pixels was obtained during the manual selection of the bore front interface with the dry ground in the images due to image blur related to the maximum available shutter speed of the cameras and the occasional difficulty to determine the bore front correctly on the previously wetted surface. Pixel-to-real-world coordinate ratios varied based on the non-orthographic angular field of view covered by the cameras. Values ranging from 6.41–10.74 pixels/cm in the x-direction and 5.59–5.92 pixels/cm in the y-direction were obtained. Thus, the SI-unit-based accuracy of the manual bore front selection process was determined to be in the range of 0.01–0.02 m in the x-direction and 0.02 m in the y-direction.

Fig. 5 shows the propagation of the bore front for the length of the experimental run. The elongated solitary wave profile (shown in Fig. 4) broke at the vertical quay and subsequently propagated as a turbulent bore, with the front parallel to the edge of the apron. The propagation of the front continued until it reached the container models (green rectangles). On initial impact with the debris, little debris movement occurs causing a buildup of water behind them. Water continues to build up behind the debris until their movement is initiated. Further on, the water entrains the debris within the propagating bore and the bore front accelerates, lagging slightly behind the bore front unaffected by the debris – along the lateral sides of the debris (Fig. 5(a)). The lag of the bore front is due to the accumulation of the debris in the bore front (Matsutomi et al., 2008). The debris slowly fall behind the accelerating bore front, similar to Yao et al. (2014). The complex interplay of debris and the bore for a varying number of container models was analysed closer in Stolle et al. (2015) and the development of a bow-like wave (Goseberg and Schlurmann, 2014; Bremm et al., 2015) on impact of the bore front was found for all investigated debris arrangements. Due to the horizontal non-inclined apron, the rundown of a bore could not be observed, but further research seems necessary to investigate how varying inclinations of the initially dry ground would affect the entrainment and advection processes. In addition, the lag of the bore front increases in the region where the debris are propagating, creating thus a bow-shaped bore front. This in turn suggests that the reciprocal influence of incoming bore front and debris entrainment is a rather continuous process which, under steady-state conditions, would only cease after the bore front and debris' relative velocity approaches zero.

When the obstacles (black squares) were placed on the apron, there is a significant change in the bore front characteristics (Fig. 5(b)–(c)). As the bore front reaches the obstacles, the water builds up in front of the obstacles and a jet forms between the obstacles as was also observed by Goseberg and Schlurmann (2014) for run-up and wake angle studies on a 1:40 sloping beach. The jet between the columns appears to change from sub-critical to super-critical flow and a turbulent wake begins to form behind the obstacles. As the bore continues to propagate, the wake begins to close in behind the obstacle. For one row of obstacles, the wake closes approximately 0.5 m downstream of the obstacles. For two rows of obstacles, the second row (located 0.45 m downstream of first row) again obstructs the closing of the wake, resulting in the bore not reforming for another 0.5 m downstream.

The jet feature is exaggerated when the debris are caught against the obstacles. This is particularly noticeable at the central obstacle as the center of the debris directly contacts the obstacles and is caught against the column by the incoming flow. When the debris are caught against the obstacle, the width of the obstruction is increased further restricting the bore propagation and resulting thus in even higher accelerations of the jet. The features of the debris caught in front of obstacles aligns well with studies of woody debris caught at bridge piers which increase the

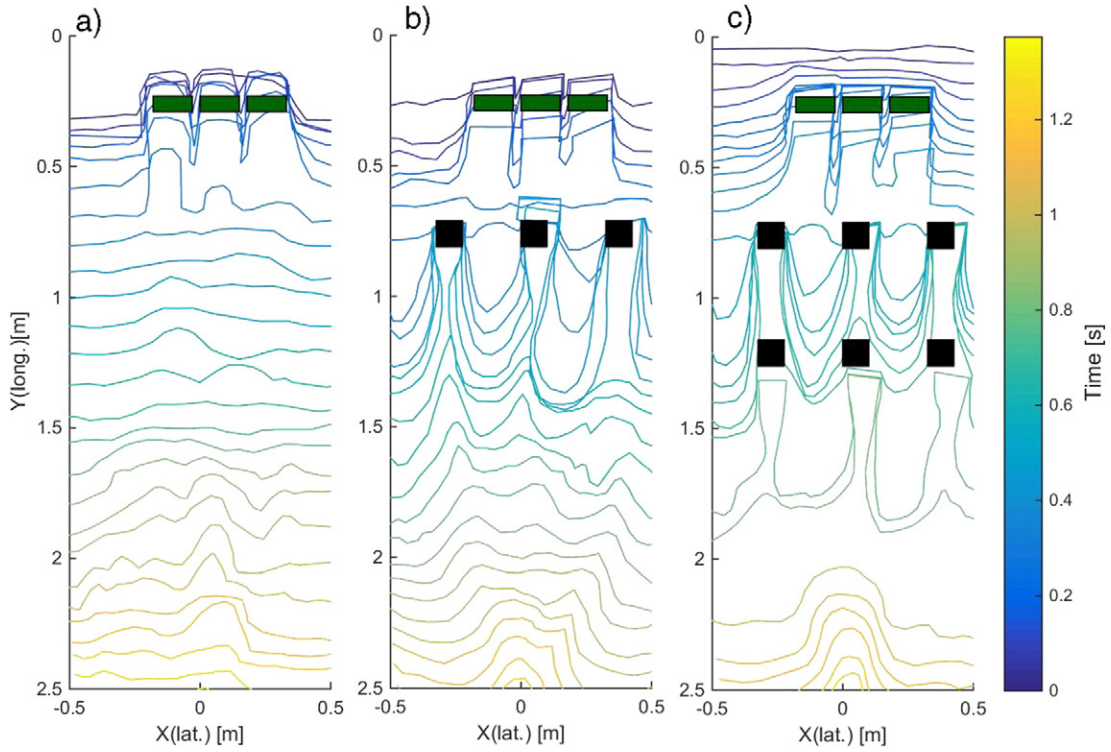

Fig. 5. Bore front profile analysis. Shows the time-history of the bore front through Experiment 34. Initial position of the debris (green rectangle) and the obstacles (black square) are superimposed on the bore front profile.

tendency of scouring and amplified flow velocities (Melville and Dongol, 1992; Schmocker and Hager, 2011). The increased turbulence caused by the restrictions through the obstacles results in the bore front affected by the debris movement to fall further behind the unaffected bore front. Due to the fixed obstructions to the debris propagation, the debris fall even further behind the propagating bore front, resulting in the smaller longitudinal displacement as described in Section 3.3.

The presence of the highly turbulent flow as a result of the breaking wave and the channelization of the flow result in some potential scale effects. As turbulence cannot properly be scaled using Froude similitude (She and Leveque, 1994), the direct effects of turbulence at prototype scale will be significantly different than those occurring at model scale. The relative turbulence eddy scale to debris size likely results in effects on the orientation of the debris that would not be observed at a larger scale. Additional scale effects, such as those induced by the unscaled air bubbles in the advancing bore front (Chanson, 2009) and the magnitude of potential multi-debris impact, highly dependent on the stiffness of the debris (Haehnel and Daly, 2004), under such conditions are challenges which need further investigation.

3.3. Debris motion description

3.3.1. Maximum longitudinal displacement

The debris motion is quantified using two quantitative parameters: the maximum longitudinal displacement and the spreading angle. The maximum longitudinal displacement (d_{lon}) is the maximum displacement, in meters, along the direction perpendicular to the apron edge between the initial position of the debris and their final position. The spreading angle (θ) is the angle, in degrees, measured between the x-axis of the system of coordinates and a line connecting the origin of the system of coordinated and the final position of the debris. Both parameters are defined graphically in Fig. 1. The parameters are compared to the fitted equation from Nistor et al. (2016); the authors used the same experimental setup except without obstacles present on the apron area. Nistor et al. (2016) determined that the maximum longitudinal displacement negatively correlated with the number of debris in the experiment (shown in Eq. (3)) and also provided an envelope, indicating the outermost positive and negative x-position of the debris, for the spreading angle (Eq. (4)). The fitted equations are a function of the number of debris (N) in the experiment:

$$d_{lon} = 3.58 - 0.09N \tag{3}$$

$$\pm\theta = \pm 3.69 \pm 0.80 \cdot N \tag{4}$$

The longitudinal displacement of the debris for each of the categories with six pieces of debris, outlined in Table 2, is presented in Fig. 6.

As shown in Fig. 6, the cases with obstacles have significantly smaller longitudinal displacements when compared to both the experiments with no obstacles and to the fitted data from Nistor et al. (2016). Obstacles act as an obstruction to both the debris and the inundating bore; a loss of downstream kinetic energy occurs when the debris contacts the obstacles as well as a loss of momentum of the inundating flow through energy loss as it propagates through the forming wake behind the obstacles. This loss of energy is a direct result of the impact with obstacles. Flow filament curvature around the obstacles changed from sub- to supercritical flow (and vice versa) and wake generation and lateral wake interaction was observed. Goseberg (2013) evaluated the flow of long waves through obstacles while surging up a sloping beach and determined that the rapid acceleration and deceleration of the flow due to the constriction and widening of the flow path along with greater turbulence through the obstacles resulted in that loss of momentum. The loss of momentum of the incoming flow can be particularly observed by examining the experimental categories in which the debris are placed further downstream, see Table 2 (No Obstacles (Downstream) and Two Rows of Obstacles (Downstream), see last two point clouds). There is already significant momentum loss due to bottom friction and turbulence within the bore as the bore propagates over the 1.81 m as result of moving the debris further downstream. However, when the two

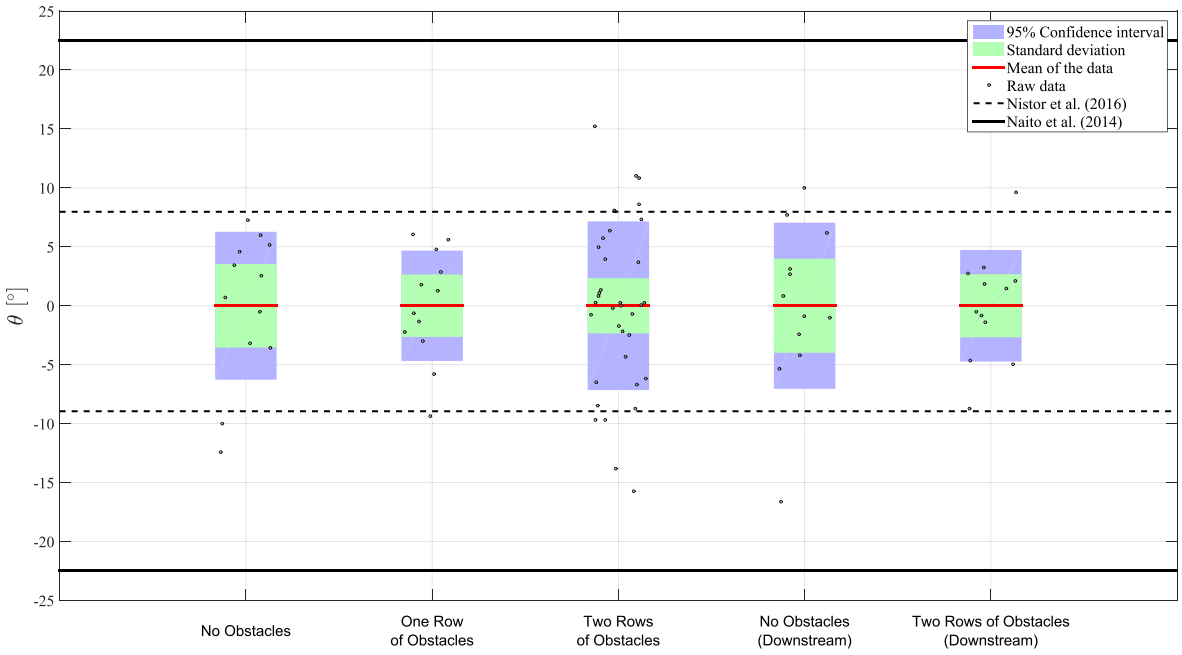

Fig. 6. Maximum longitudinal displacement of debris units. Mean (red), standard deviation (blue) and 95% confidence intervals (green) indicate statistics of the data per debris number cluster. Fitted data (black dotted line) from Nistor et al. (2016).

rows of obstacles are present there is a significant loss of momentum resulting in the smaller longitudinal displacement observed in *Two Rows of Obstacles* (*Downstream*).

While obstacles have a significant effect in limiting the longitudinal displacement, the difference in adding a second row of obstacles is limited. As shown in Fig. 6, the difference in the mean longitudinal displacement is −1.05 m between no obstacles and one row of obstacles but only −0.31 m between one row of obstacles and two rows which appear comparatively less significant given the rather large standard deviation for these cases of approximately ±0.7 m. The difference in the effect of the row of obstacles is primarily due to the arrangement of the second row. As discussed in Section 3.2, the wake which occurred behind the first row of obstacles does not reform thereafter as it is already affected by the second row of obstacles. The debris are mostly entrained within the jet-like flow in between the obstacles and therefore will likely follow the flow path, which passes between the them. This results in the debris being rarely caught by the second row of obstacles and often not contacting them at all. An adjustment to the arrangement of the obstacles, by staggering the second row or leaving a wider space between the first and second row, would likely improve the influence of the second row in limiting the longitudinal displacement of the debris.

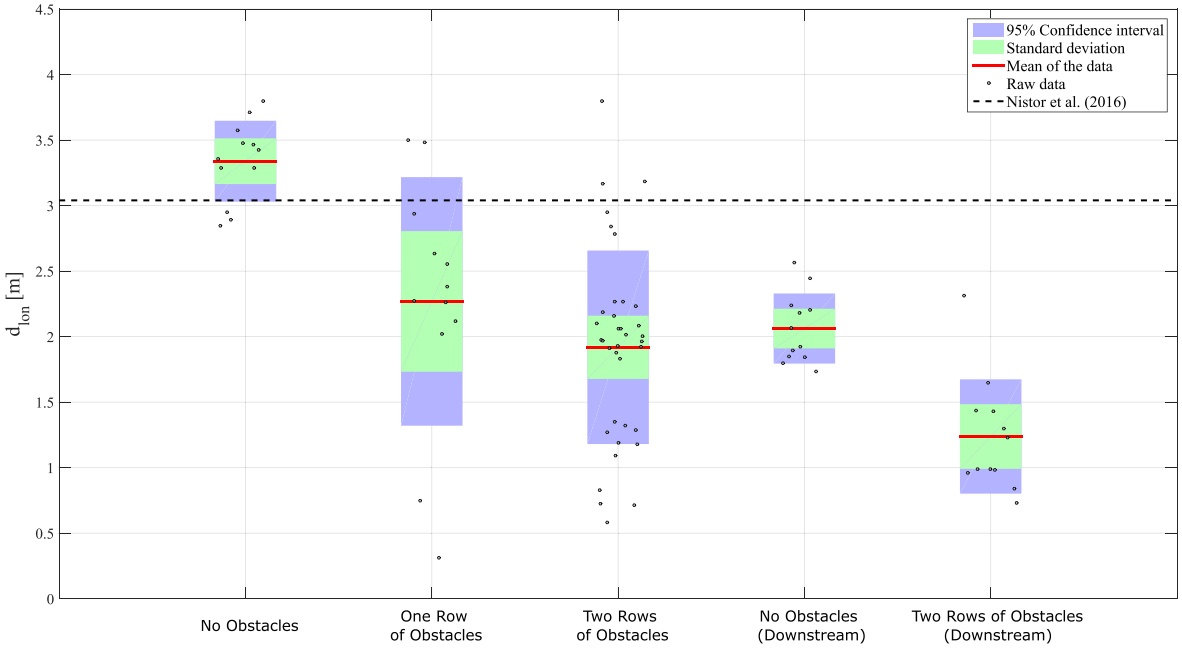

Fig. 7. Positive and negative spreading angle (θ). Mean (red), standard deviation (blue) and 95% confidence intervals (green) indicate statistics of the data per debris number cluster. Fitted data (black dotted line) from Nistor et al. (2016).

3.3.2. Spreading angle

The spreading angle for each of the categories with six containers, outlined in Table 2, is displayed in Fig. 7. As can be observed, the majority of the debris spreading angle are within the fitted data from Nistor et al. (2016) shown as a dashed line. All data is well within the ±22.5° spreading angle envelope determined from field surveys performed by Naito et al. (2014). The obstacles appear to have little effect on the spreading angle. However, the outliers that can be observed for the *Two Rows of Obstacles* are a result of a physical process whereas the debris get entrained within the wake occuring behind the second row of obstacles. Due to the turbulent flow conditions between the obstacles, the process occurred only in specific situations and resulted in a significantly higher spreading angle.

Table 3 summarizes the parameters that describe the motion of the debris on a horizontal apron area after being propelled by an incoming tsunami-like bore in terms of maximum longitudinal displacement and spreading angle along with the major differences between the cases where no obstacles are present on the apron area.

3.3.3. Debris-obstacle collision process and effects

Fig. 8 shows the process and steps involved that results in the rare case of increased spreading angle due to the obstacles. It shows the initial position of the debris and their corresponding movement as tracked by the RTLS system. Due to the small errors associated with tracking the debris using the RTLS system, the trajectory of the debris was approximate (±0.05 m), resulting in D3 appearing to pass through one of the obstacles. The focus here is on "Smart" debris D2 (left-most bottom container), D3 (center bottom container), and D5 (left-most top container). The typical motion of the debris was to pass between the obstacles through the centerline of the jet-like flow between the obstacles, as done by D4, D6, and D7. However in this particular case, D3 is instead caught on the second row of obstacles and further constricts the water from passing through, briefly creating a larger jet, which increases the velocity of D5. D5 contacts D2, pushing D5 into the wake that has formed behind the obstacles. The wake accelerates D5 perpendicularly to the direction of flow (y-direction) as it passes through the wake. D5 maintains a portion of the velocity in the y-direction, resulting in the significantly larger spreading angle as it is accelerated into the x-direction (lateral). Due to the specific conditions that are needed for the process to occur, only three cases of the lateral acceleration out of twelve experiments were noted. In future, more repetitions of the testing process would help in understanding the frequency in which this process occurs.

3.4. Forces exerted on container models and obstacles

The "Smart" debris system employed in the experiment contained accelerometers, which allowed for recording the accelerations of the debris. A more detailed description of the 6DOF system to monitor position and orientation over time is detailed in Goseberg et al. (2016). A similar strategy to solely record accelerations of floating objects was recently successfully implemented by Shafiei et al. (2014) who investigated floating objects in a dam-break flow. From the accelerations which were recorded at a sampling rate of 50 Hz, the forces on the debris were calculated from both the bore front and the debris impacting the fixed obstacles. The forces were normalized using the equations for calculating tsunami bore force on a vertical wall following Cross (1967):

$$F_N = \frac{1}{2}\rho g H^2 + \rho H v^2 \tag{5}$$

where ρ is the density of the fluid, H is the height of the solitary wave taken at WG2, and v is the wave-induced flow speed taken at WG2. In particular, maximum values of the wave height and flow speed which occurred at about the same time instant, were used to compute the normalization force, F_N, to yield a maximum force fully representing the incoming tsunami surge. For the force normalization, a unit width of 1 m was chosen to adequately compare the forces. Fig. 9 shows the time-history of the force (solid line) for Experiment #28 of "Smart" debris D3, which is the debris located in the center position of the configuration C1 according to Table 2. The force were calculated based on exploiting Newton's 2nd law as expressed by Eq. (6) in its vector form

$$|\boldsymbol{F}| = |\boldsymbol{a}| \cdot m \tag{6}$$

where the force vector $\boldsymbol{F}$ is the inertial force exerted on an object of mass m and its vectored acceleration $\boldsymbol{a}$. Based on the experimental results, a component-based analysis of forces through exploiting single axis acceleration recordings in the x-, y-, and z-axis was unsuccessful for the sampling frequency of 50 Hz was insufficient to fully resolve and identify sufficiently well impact events in all 3 dimensions. For this reason, the alternative approach of identifying impact events by looking at integral acceleration magnitudes was chosen. This however meant that information regarding the impact force direction at the individual contact point between the wave front and the container model or between the container model and the obstacle was irreversibly lost. Acceleration magnitudes $|\boldsymbol{a}(t)|$ were determined using the vector arithmetic exploiting Pythagorean Theorem for the component accelerations a_i with i = x,y,z as expressed by Eq. (7)

$$|\boldsymbol{a}(\boldsymbol{t})| = \sqrt{a_x{}^2 + a_y{}^2 + a_z{}^2} \tag{7}$$

The impact of the container at the structure is shown by the vertical dashed line and the inset shows the position of the container at impact with the obstacle, with the white arrow indicating the impact axis of the container. The impact of the bore front on the container at its initial position is however indicated by a dotted line occurring 0.2 s before the container model hits the first row of obstacles. The time for the impact of the container and the impact of the bore front were determined using images recorded by the two cameras mounted above the TWB. Due to the potential for spurious spikes in the acceleration as the containers were placed in their initial position or from background noise, the cameras were set to identify the correct section of the dataset for analysis. However, as can be observed in Fig. 9, the impact and arrival time did not correspond directly with the peak force signal. Due to the relatively small frame rate of the cameras (25 fps), they did not capture the moment of impact as debris impacts are of the order of 10^{-3} to 10^{-2} s. To avoid missing the impact, the image immediately before the impact was chosen if the impact

Table 3
Summary of results for the debris motion parameters.

	No obstacles	One row of obstacles	Two rows of obstacles	No obstacles (downstream)	Two rows of obstacles (downstream)
Mean d_{lon}	3.34	2.27	1.92	2.06	1.24
σ d_{lon}	0.31	0.95	0.74	0.27	0.44
%-Difference	–	32.05	42.53	38.25	62.93
Maximum pos. spreading angle	7.26	6.08	15.21	9.97	9.63
Maximum neg. spreading angle	−12.43	−9.36	−15.76	−16.64	−8.72
σ Spreading angle	4.51	4.68	7.15	7.05	4.73

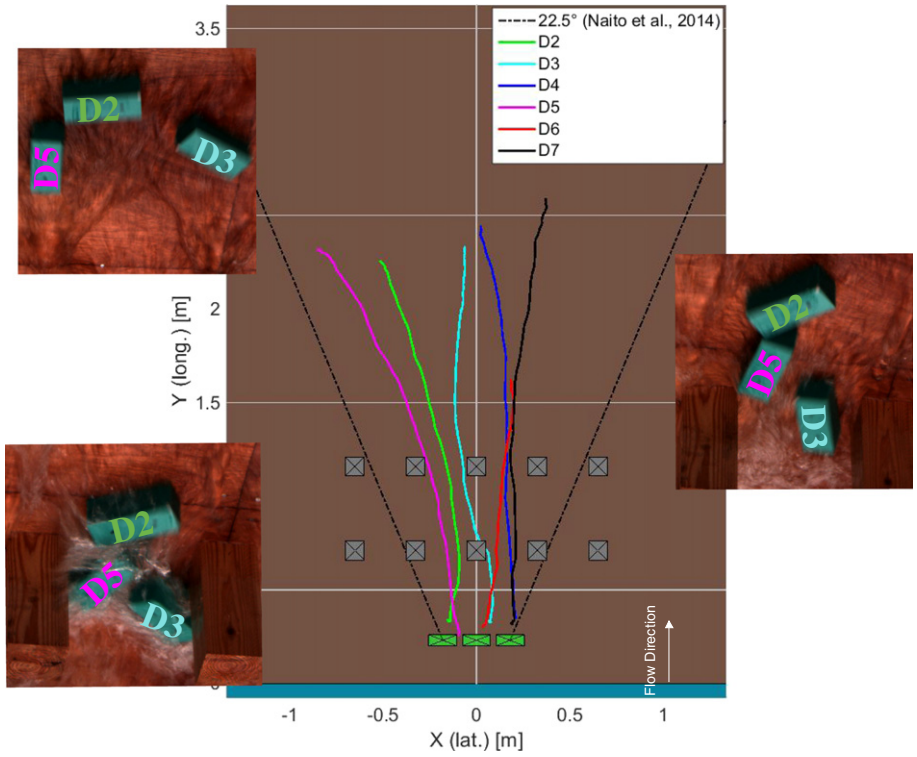

Fig. 8. Debris motion results from Experiment 36. The motion of the debris is from the RTLS data. The green boxes are the initial position of the debris and the grey squares are the obstacles. D2 and D5 are the left-most stack, D3 and D6 are the center stack, and D4 and D7 are the right-most stack. The block dashed line is the maximum spreading angles depicted by Naito et al. (2014). Insets indicate debris ID's (colour-coded) at various time instants.

was not obvious. Additionally, the synchronization between the motions sensors and the cameras was dependent on the NTP protocol which resulted in a relatively small accuracy (~30 ms) in the time signal lag between the instruments.

It is apparent that the relative impact forces exerted on the obstacle are rather small compared with the tsunami bore force potential expressed by Eq. (5). Peak forces are approximately one tenth of a percent of the force potential of the incoming bore; such order of magnitude difference is however not unrealistic as the acceleration distance between the debris' original site and the impact position is very short (0.48 m) and momentum transfer requires some time. Next, the container model which was entrained in the bore resulted a small amount of the potential force as the equation by Cross (1967) originally was intended to describe the force of a solitary wave exerted on a vertical wall per unit widths and with maximum wave height, *H*. In this case, the wave only hits an object of much smaller front surface. What is however notable is that the sequence of force impacts is well preserved in its temporal evolution. Future research has yet to look into the minimum sampling frequency required to fully resolve force spikes at debris impact as the sampling frequency with which the accelerometers were operated was probably too small for these event durations to be properly captured.

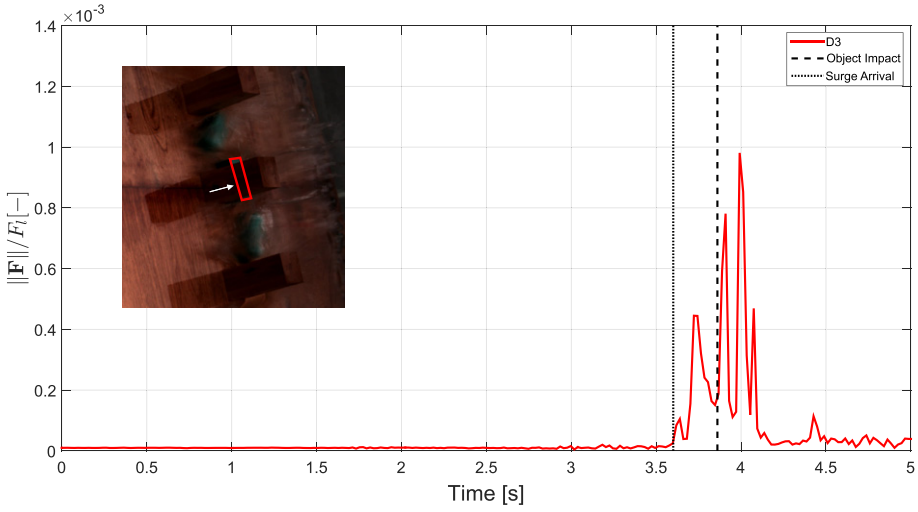

Fig. 9. Force time-history for D3 (center debris) in Experiment 28. The dotted line is the impact time as derived from the camera data. Forces are normalized from Cross (1967). Photo inset shows instant of debris impact.

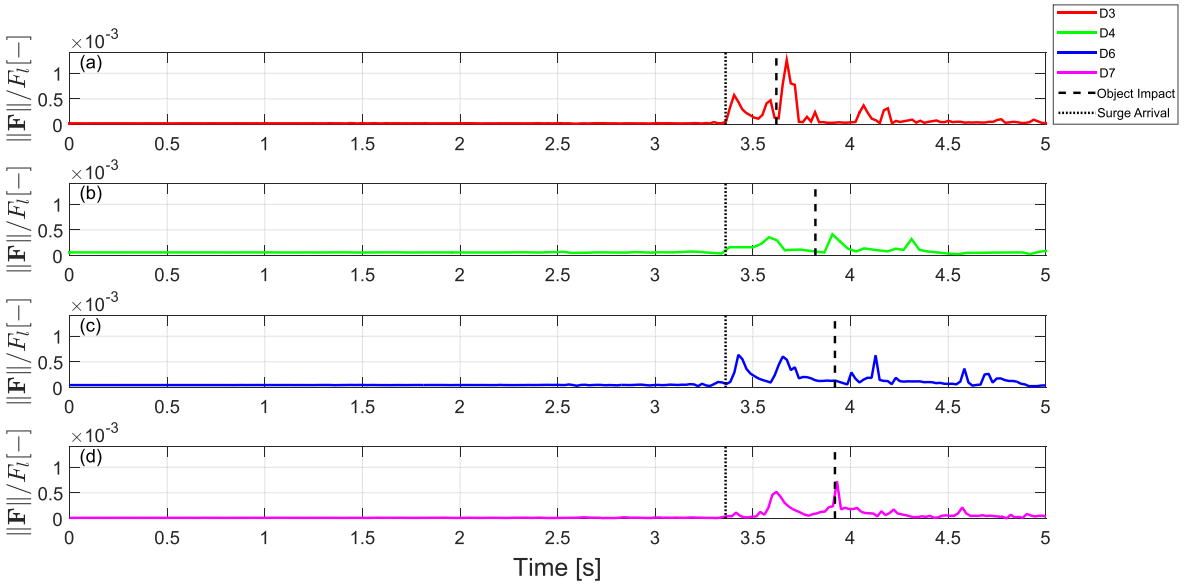

Fig. 10. Force-time history from Experiment 30. (a) D3 (bottom layer) and (c) D6 (upper layer) are the stacked center debris and (b) D4 (bottom layer) and (d) D7 (upper layer) are the outermost stacked debris in the positive x-direction (see Fig. 1). Forces are normalized from Cross (1967). The white arrow in the inset represents the approximate impact point of the debris and the fixed obstacles.

Fig. 10 additionally highlights normalized magnitude force time-histories of four concurrently propagating container models equipped with "Smart" debris equipment with time zero referring to the instant in time when the wave maker was initiated. Fig. 11 supplements the magnitude force time-histories by showing the camera-captured images at the impact times indicated in Fig. 10 by the dashed lines sometime after the bore front arrived at the obstacles.

The Experiment C4 shown in Fig. 10 contains 6 container models being propelled through two rows of obstacles and of which 4 were equipped with motion sensors recording linear accelerations (gravity-independent). As synchronization between all the instrumentation was generally very favorable, different force time-histories are comparable by this means and it becomes possible to identify which of the notable force spikes originate from inter-debris or obstacle-debris impacts. The first panel of Fig. 10 presents the magnitude force time-history of D3 which was initially positioned centered, bottom layer in this debris arrangement. It becomes apparent, that two distinct force peaks are evident from the time-history of which the first can be attributed to the arrival of the tsunami bore and the second happened around the impact time when the debris struck the center obstacle of the first obstacle row.

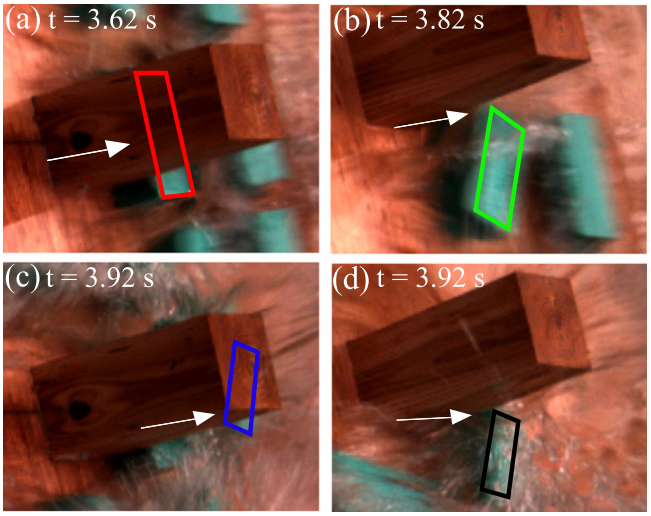

Fig. 11. Initial impact of debris on the obstacles for data presented in Fig. 10. The impact frames of each debris (a) D3, (b) D4, (c) D6, and (d) D7. The white arrow represents the approximate impact point of the debris and the fixed obstacles.

As shown in Fig. 11(a), D3 underwent a frontal impact which effectively decelerated the debris' velocity to zero in a short instant of time, thus leading to a large impact force. The time elapsed between the arrival of the bore front and the subsequent impact of the debris with the obstacle was estimated at 0.3 s, indicating that the debris had fallen some distance behind the actual bore front. The temporal resolution of the acceleration data which was used to compute inertial force magnitudes is inadequate, as the force peaks are only resolved by few data points. It becomes clear that follow-up studies would benefit from using increased sampling rates for the accelerometers. Fig. 10(b) and Fig. 11(b) depict the inertial force time-history and its impact scene of D4 which was different from D3 by being positioned at the bottom layer outer stack of the debris arrangement. The inertial forces measured on the debris are slightly smaller around the time of the bore front arrival, but what is most notably is that there is a much smaller impact force following the impact's instant of time. This can however be explained by the fact that D4 hit the obstacle while not being oriented directly through its center of inertia as shown in Fig. 11(b) presumably resulting in smaller force peaks. Tangential impact vectors or impacts at large angles deviating from the flow normal were already found to reduce impact forces in the work of Haehnel and Daly (2004). Time between bore front arrival and the impact is 0.5 s and thus slightly larger than for debris D3. Fig. 10(c), (d) and Fig. 11(c), (d) present magnitude force time-histories and the images at impact instants of time for the upper layer, D6 and D7. In contrast to the two, D3 and D4 positioned at the bottom layer, time lags between the bore front arrival and the impact are increased to 0.6 s for both upper layers of debris. This increase is caused by the entrainment process that significantly differs for the bottom and upper layer of the debris. Based on video observations, the bottom layer of debris motion was predominantly initiated through the approaching bore front build-up at the debris' front face which led to an entirely horizontal force and a sliding motion out underneath the upper layer debris was the result. At this time, the upper layer of debris had not experienced any force other than a small friction force (exerted between the upper side of the bottom debris and the lower side of the upper debris) during the slip of the bottom layer debris out

of its debris stack. As a result of the friction force and the gravitational acceleration on the upper layer of debris, its motion was backwards rotating, falling towards the incoming bore. The upper layer of debris thus got into contact with the bore some time later than the bottom layer of debris delaying the inevitable impact with the obstacles. As shown in Fig. 11(d), D7 struck the obstacle under an angle similar to the one of D4 shown in Fig. 11(b), thus leading to a larger impact force as indicated by the dashed line in Fig. 10(d). It however seems likely that the higher water level around D7 leads to an added mass effect which was oftentimes found to increase hydrodynamic and impact forces in literature (Isaacson and Cheung, 1988; Landweber and Shahshahan, 1992).

4. Discussion

In this study, a solitary wave was used despite the fact that the authors are fully aware of the discussion regarding the discouragement of solitary waves by Madsen et al. (2008) in the context of tsunami research. As such, the application of generic, classical solitary waves in the context of tsunami run-up, or propagation was recently challenged (Madsen et al., 2008) for their spatial and temporal scaling which rarely matches typical real tsunami features and order of magnitude errors could occur in cases where scaling issues were not thoroughly addressed. Nevertheless, there is well-justified grounds to use waves with solitary wave front profiles to investigate near-shore coastal problems such as impact and debris transport studies. More recently, elongated waves with solitary wave profiles were successfully generated by a pump-driven wave generator (Goseberg et al., 2013) and applied to macro-roughness wave interaction in a laboratory (Goseberg, 2013). Length and time scale as well as surface tension issues of experimental tsunami-shoreline interaction were further discussed in Bremm et al. (2015), Goseberg (2013) and Drähne et al. (2016).

Irrespective of all ongoing discussion with regard to the appropriate representation of near-shore tsunami effects and its hydrodynamics, there is a large body of research which arguably well adopted solitary waves to study near-shore impact and debris transport (Chinnarasri et al., 2013; Strusinska-Correia et al., 2013; Esteban et al., 2014; Seiffert et al., 2014; Yao et al., 2014). Madsen et al. (2009) deduce with a higher order Boussinesq model that the appearance of undular bores at the front of a tsunami propagating over a continental shelf and shoaling towards the shoreline is very likely. Those shorter waves undoubtedly have a much greater influence on impact loads and initial surging forces on coastal infrastructure. Moreover, Madsen et al. (2008) report on the grounds of eye-witness reports and photographs of the 1983 Nihonkai-Chubu tsunami wave periods of 10–15 s; this fact was equally confirmed for the 2004 Indian Ocean tsunami. And, it is explicitly stated that these short waves have a "local additional effect on wave impact on coastal structures" (Madsen et al., 2008) which is why this study involves elongated solitary waves to mimic the short duration tsunami front behavior with very comparable wave periods (about 30 s as mentioned in section "Hydrodynamics of the elongated solitary wave") in the range of the stated short wave durations of the undulations.

In order to rule out biasing scale effects related with the influence of the surface tension on the tsunami surge propagating over the horizontal apron, Weber numbers (We) were compared with accepted critical thresholds given in literature to assess if the debris transport process was impaired. The Weber number is defined as:

$$\mathrm{We} = \frac{\rho v^2 l}{\sigma} \tag{8}$$

where $\rho = 1000$ kg/m^3 is the fluid density, v is the fluid speed at some location on the apron, l is a characteristic length scale (here the fluid depth at said location), and σ is the surface tension for 20 °C water (Peakall and Warburton, 1996; Bremm et al., 2015). Fluid speed over the apron responsible for the entrainment and transport of the debris was found to be in the range of $v = 1$–2 m/s while the depth of the fluid layer propagating over the apron was of at least $l = 0.025$ m as this was the required fluid depth to initiate floatation of the debris. These assumptions yielded Weber numbers in the range of We = 342–1269 which exceed critical thresholds of $\mathrm{We}_{\mathrm{crit}} = 2.5$–$160$. Biasing scale effects through surface tension can thus be ruled out to the greatest extent in this research.

While the hydrodynamic conditions adequately model the incipient motion of the debris, the shorter duration waves inevitably influence the longitudinal displacement of the debris. As a result, the longitudinal displacement cannot be directly compared to the method proposed by Naito et al. (2014). However, the influence of the fixed obstacles on the longitudinal displacement can be assessed by comparison to the results presented by Nistor et al. (2016). The presence of the obstacles within the flow significantly reduced the longitudinal displacement of the debris by acting as an obstacle to the propagation of the debris. Additionally, the obstacles acted as a macro-roughness element (Goseberg, 2013), inhibiting the momentum of the wave and therefore reducing the momentum transfer to the debris.

The work presented herein presents for the first time an attempt to categorize potential interaction between entrained positively buoyant debris displaced during extreme hydrodynamic flows as represented by a tsunami-like bore flow and arrangements of obstacles onshore. It is acknowledged that the following parameters will surely have a significant influence on the chosen metric parameters 'maximum longitudinal displacement' and 'spreading angle', which is (a) the obstruction ratio on the obstacles in the lateral direction as successfully shown by Goseberg (2013) for fluid-only flows, (b) the number of obstacle rows involved in the bore process, (c) the hydrodynamic force available to initially displace and propel any debris present at an onshore site prone to tsunami inundation; and (d) bed slope. In this regard, future research deems necessary as the amount of time to accomplish the required experimental work clearly exceeds the scope of the current study.

5. Summary and conclusions

The presented experimental research was directed towards elucidation of mechanisms of debris motion over a horizontal apron area representing a typical harbor layout flooded by an incoming tsunami and focussed towards debris interaction with solid obstacles in non-staggered (aligned) environments. As an idealization to the very complex prototype situation conceivable, debris were modelled by using 20-foot shipping container models at a 1:40 length scale in geometric scale which propagated over an ideally horizontal surface. The wave propagation section and the harbor apron area were separated by a vertical quay wall which allowed the incoming elongated solitary wave to steepen, break and propagate over the initially dry surface as a tsunami bore. In its path of propagation, a varying number of container models were entrained in the resulting flow, propelled and they eventually interacted with regularly spaced vertical obstacles. Some debris and obstacle arrangements were basically tested to elucidate the effects the aligned obstacles would have on the debris' maximum longitudinal displacement and the spreading angles. The presented data set of debris-obstacle interaction and the adjacent analysis may serve to calibrate and test numerical models that unlike experimental tests allow for investigating more diverse obstacle combinations in the future. Based on the given set-up, the following conclusions are drawn with regard to the bore front response to the debris and the debris motion itself:

- The hydrodynamics of the incoming elongated solitary wave chosen herein resemble well those short riding waves which often occur in combination with rather long tsunami wave propagating and shoaling over the continental shelf towards the shore; the riding waves are a product of wave fission at the tsunami front leading to short waves with periods of 10–30 s in nature (undulating bores) which will most likely govern the impact to and of dislodged

material on the nearby surrounding. The research is thus limited to this region starting at the shoreline and stretching some hundred meters inland where immediate impacts with other infrastructure might occur.

- The bore front over the apron area was significantly deformed for cases with container models placed; the transfer of momentum from the bore front leading to entrainment and acceleration of the container models resulted in the bore front lagging behind the undisturbed sections of the bore front. At the same time, additional obstacles interacting with the incoming bore front resulted in focussing and channeling of energy through the gaps between the obstacles; those processes concurrently affected the transport of the debris within the extreme flow.
- Compared to existing findings about the maximum longitudinal displacement of debris, it was found that a first row of obstacles significantly reduced this parameter. However, it is remarkable that the addition of a second row of obstacles had only limited effect on the maximum longitudinal displacement of container models. This is explained by the fact that a first row of obstacles led to channelized flow directing and guiding the entrained debris through the spacing between the second row obstacles rather than directly impacting them, as the second row of obstacles was not staggered.

Conversely, the parameter 'spreading angle' was relatively unaltered when compared with an unobstructed harbor apron area. The variation found for the dispersal of the container models in the flow was insignificant to draw any reliable conclusions from it: this remains to be proven through future work involving additional numbers of repetitions. Larger or smaller amounts of debris, as well as variations of obstacle arrangements, will potentially alter the spreading angle of dislodged material.

Likewise, until further research renders available, planners and designer may conclude that debris spreading is not likely to be modified by the presence of rigid obstacles. Thus, spreading angles and maximum longitudinal displacement define debris-impact zones which are required by designers to determine maximum loading conditions of buildings situated in the relevant settings covered by this research. Validity of the current research covers configurations with aligned obstacles and future research needs to investigate how further obstacle configurations could change maximum longitudinal displacement and spreading angles.

— Finally, inertial forces were determined for selected cases involving 3 and 6 container models. By means of the "Smart" debris system installed inside the container models it became possible to evaluate the inertial forces exerted to the debris itself and to the obstacles during the collision process which randomly happened during the experiments. Forces were found to be small compared with forces found to be exerted on vertical walls from solitary waves as given by Cross (1967).

References

Arnason, H., Petroff, C., Yeh, H., 2009. Tsunami bore impingement onto a vertical column. J. Disaster Res. 4, 391–403.

Bocchiola, D., Rulli, M., Rosso, R., 2006. Transport of large woody debris in the presence of obstacles. Geomorphology 76, 166–178.

Bremm, G.C., Goseberg, N., Schlurmann, T., Nistor, I., 2015. Long wave flow interaction with a single square structure on a sloping beach. J. Mar. Sci. Eng. 3, 821.

Chanson, H., 2009. Current knowledge in hydraulic jumps and related phenomena. A survey of experimental results. Eur. J. Mech.-B/Fluids 28, 191–210.

Chinnarasri, C., Thanasisathit, N., Ruangrassamee, A., Weesakul, S., Lukkunaprasit, P., 2013. The impact of tsunami-induced bores on buildings. Proc. Inst. Civ. Eng. 166, 14–24.

Coulbourne, W.L., 2011. ASCE 7-10 changes to flood load provisions. Proceedings Structures Congress 2011. ASCE, pp. 1411–1417.

Cross, R.H., 1967. Tsunami surge forces. J. Waterw. Harb. Div. 93, 201–234.

Dias, F., Dutykh, D., 2007. Dynamics of tsunami waves. Extreme Manmade Natural Hazards Dynamics Structures. Springer, pp. 201–224.

Drähne, U., Goseberg, N., Vater, S., Beisiegel, U., Behrens, J., 2016. An experimental and numerical study of analytical solutions for tsunami run-up on a plane beach. J. Mar. Sci. Eng. 4.

Esteban, M., Jayaratne, R., Mikami, T., Morikubo, I., Shibayama, T., Thao, N.D., Ohira, K., Ohtani, A., Mizuno, Y., Kinoshita, M., Matsuba, S., 2014. Stability of breakwater armor units against tsunami attacks. J. Waterw. Port Coast. Ocean Eng. 140, 188–198.

Esteban, M., Takagi, H., Shibayama, T., 2015. Handbook of coastal disaster mitigation for engineers and planners. Handbook of Coastal Disaster Mitigation for Engineers and Planners.

FEMA P-55, 2011. Federal Emergency Management Agency.

Ghobarah, A., Saatcioglu, M., Nistor, I., 2006. The impact of the 26 December 2004 earthquake and tsunami on structures and infrastructure. Eng. Struct. 28, 312–326.

Goseberg, N., 2013. Reduction of maximum tsunami run-up due to the interaction with beachfront development - application of single sinusoidal waves. Nat. Hazards Earth Syst. Sci. Disc. 1, 1119–1171.

Goseberg, N., Schlurmann, T., 2014. Non-stationary flow around buildings during run-up of tsunami waves on a plain beach. Coast. Eng. Proc. 1, 21.

Goseberg, N., Wurpts, A., Schlurmann, T., 2013. Laboratory-scale generation of tsunami and long waves. Coast. Eng. 79, 57–74.

Goseberg, N., Nistor, I., Mikami, T., Shibayama, T., Stolle, J., 2016. Nonintrusive spatiotemporal smart debris tracking in turbulent flows with application to debris-laden tsunami inundation. J. Hydraul. Eng. 04016058.

Haehnel, R.B., Daly, S.F., 2004. Maximum impact force of woody debris on floodplain structures. J. Hydraul. Eng. 130, 112–120.

Imamura, F., Goto, K., Ohkubo, S., 2008. A numerical model for the transport of a boulder by tsunami. J. Geophys. Res. Oceans 1978–2012, 113.

Isaacson, M., Cheung, K.F., 1988. Influence of added mass on ice impacts. Can. J. Civ. Eng. 15, 698–708.

Khan, A.A., Steffler, P.M., Gerard, R., 2000. Dam-break surges with floating debris. J. Hydraul. Eng. 126, 375–379.

Knörr, W., Kutzner, F., 2008. EcoTransIT: Ecological Transport Information Tool - Environmental Method and Data. IFEU, Heidelberg.

Landweber, L., Shahshahan, A., 1992. Added masses and forces on two bodies approaching central impact in an inviscid fluid. J. Ship Res. 36, 99–122.

Madsen, P.A., Fuhrman, D.R., Schäffer, H.A., 2008. On the solitary wave paradigm for tsunamis. J. Geophys. Res. Oceans 113.

Madsen, P.A., Fuhrman, D.R., Schaffer, H.A., 2009. A Critical Discussion of the Solitary Wave Paradigm for Tsunamis, in: Smith, J.M. (Ed.), CoastalEngineering2008. pp. 1262–1274.

Matsutomi, H., 2009. Method for estimating collision force of driftwood accompanying tsunami inundation flow. J. Disaster Res. 4, 435–440.

Matsutomi, H., Fujii, M., Yamaguchi, T., 2008. Experiments and development of a model on the inundated flow with floating bodies. Coast. Eng. 1458–1470.

Melville, B., Dongol, D., 1992. Bridge pier scour with debris accumulation. J. Hydraul. Eng. 118, 1306–1310.

Munk, W.H., 1949. The solitary wave theory and its application to surf problems. Ann. N. Y. Acad. Sci. 51, 376–424.

Nafziger, J., She, Y., Hicks, F., 2016. Celerities of waves and ice runs from ice jam releases. Cold Reg. Sci. Technol. 123, 71–80.

Naito, C., Cercone, C., Riggs, H.R., Cox, D., 2014. Procedure for site assessment of the potential for tsunami debris impact. J. Waterw. Port Coast. Ocean Eng. 140, 223–232.

Nistor, I., Palermo, D., Cornett, A., Al-Faesly, T., 2011. Experimental and numerical modeling of tsunami loading on structures. Coast. Eng. Proc. 1, 2.

Nistor, I., Goseberg, N., Mikami, T., Shibayama, T., Stolle, J., Nakamura, R., Matsuba, S., 2016. Hydraulic experiments on debris dynamics over a horizontal plane. J. Waterw. Port Coast. Ocean Eng. in press.

Nouri, Y., Nistor, I., Palermo, D., Cornett, A., 2010. Experimental investigation of tsunami impact on free standing structures. Coast. Eng. J. 52, 43–70.

Okal, E.A., Fritz, H.M., Synolakis, C.E., Borrero, J.C., Weiss, R., Lynett, P.J., Titov, V.V., Foteinis, S., Jaffe, B.E., Liu, P.L.-F., Chan, I., 2010. Field survey of the Samoa tsunami of 29 September 2009. Seismol. Res. Lett. 81, 577–591.

Palermo, D., Nistor, I., Nouri, Y., Cornett, A., 2009. Tsunami loading of near-shoreline structures: a primer. Can. J. Civ. Eng. 36, 1804–1815.

Palermo, D., Nistor, I., Saatcioglu, M., Ghobarah, A., 2013. Impact and damage to structures during the 27 February 2010 Chile tsunami 1. Can. J. Civ. Eng. 40, 750–758.

Peakall, J., Warburton, J., 1996. Surface tension in small hydraulic river models – the significance of the Weber number. J. Hydrol. 53, 199–212.

Ramsden, J.D., 1996. Forces on a vertical wall due to long waves, bores, and dry-bed surges. J. Waterw. Port Coast. Ocean Eng. 122, 134–141.

Rueben, M., Cox, D., Holman, R., Shin, S., Stanley, J., 2014. Optical measurements of tsunami inundation and debris movement in a large-scale wave basin. J. Waterw. Port Coast. Ocean Eng. 141.

Rusyda, M.I., Hashimoto, H., Ikematsu, S., 2014. Log jam formation by an obstruction in a river. Proc. Fluvial Hydraul. RIVER FLOW 2014, 717–724.

Schmocker, L., Hager, W., 2011. Probability of drift blockage at bridge decks. J. Hydraul. Eng. 137, 470–479.

Seiffert, B., Hayatdavoodi, M., Ertekin, R.C., 2014. Experiments and computations of solitary-wave forces on a coastal-bridge deck. Part I: Flat Plate. Coast. Eng. 88, 194–209.

Shafiei, S., Melville, B., Beskhyroun, S., Shamseldin, A., 2014. Preliminary investigation of the tsunami-borne debris impact on structures: a new method for impact force measurement. 5th IAHR International Symposium Hydraulic Structures. The University of Queensland, pp. 1–9.

She, Z.-S., Leveque, E., 1994. Universal scaling laws in fully developed turbulence. Phys. Rev. Lett. 72, 336.

St-Germain, P., Nistor, I., Townsend, R., 2012. Numerical modeling of the impact with structures of tsunami bores propagating on dry and wet beds using the SPH method. Int. J. Protective Struct. 3, 221–256.
Stolle, J., Nistor, I., Goseberg, N., Mikami, T., Shibayama, T., Nakamura, R., Matsuba, S., 2015. Flood-induced Debris Dynamics Over a Horizontal Surface, in: Coastal Structures Solutions Coastal Disasters. ASCE-COPRI.
Stolle, J., Nistor, I., Goseberg, N., 2016. Optical tracking of floating shipping containers in a high-velocity flow. Coast. Eng. J. 1650005.
Strusinska-Correia, A., Husrin, S., Oumeraci, H., 2013. Tsunami damping by mangrove forest: a laboratory study using parameterized trees. Nat. Hazards Earth Syst. Sci. 13, 483–503.
Takahashi, S., Sugano, T., Tomita, T., Arikawa, T., Tatsumi, D., Kashima, H., Murata, S., Matsuoka, Y., Nakamura, T., 2010. Joint survey for 2010 Chilean earthquake and tsunami disaster in ports and coasts. Port Airport Res. Instrum.
Wei, Z., Dalrymple, R.A., Hérault, A., Bilotta, G., Rustico, E., Yeh, H., 2015. SPH modeling of dynamic impact of tsunami bore on bridge piers. Coast. Eng. 104, 26–42.
Yao, Y., Huang, Z., Lo, E.Y.M., Shen, H.-T., 2014. A preliminary laboratory study of motion of floating debris generated by solitary waves running up a beach. J. Earthq. Tsunami 8.
Yeh, H., 2009. In: Bernard, E.N., Robinson, A.R. (Eds.), The Sea - Tsunamis. Harvard University Press, pp. 333–369.
Yeh, H., Barbosa, A.R., Ko, H., Cawley, J.G., 2014. Tsunami loadings on structures: review and analysis. Coast. Eng. Proc. 1 currents–4.
Zainali, A., Weiss, R., 2015. Boulder dislodgement and transport by solitary waves: insights from three-dimensional numerical simulations. Geophys. Res. Lett. 42, 4490–4497.